Diverse electronic landscape of the kagome metal YbTi$_3$Bi$_4$

Anup Pradhan Sakhya [1,7], Brenden R. Ortiz [2,7], Barun Ghosh [3,4,7], Milo Sprague[1], Mazharul Islam Mondal[1], Matthew Matzelle[3,4], Iftakhar Bin Elius[1], Nathan Valadez[1], David G. Mandrus [2,5,6], Arun Bansil[3,4] & Madhab Neupane [1] ✉

Kagome lattices have emerged as an ideal platform for exploring exotic quantum phenomena in materials. Here, we report the discovery of Ti-based kagome metal YbTi$_3$Bi$_4$ which we characterize using angle-resolved photoemission spectroscopy (ARPES) and magneto-transport, in combination with density functional theory calculations. Our ARPES results reveal the complex fermiology of YbTi$_3$Bi$_4$ and provide spectroscopic evidence of four flat bands. Our measurements also show the presence of multiple van Hove singularities originating from Ti 3d orbitals and a linearly-dispersing gapped Dirac-like bulk state at the $\overline{\mathrm{K}}$ point in accord with our theoretical calculations. Our study establishes YbTi$_3$Bi$_4$ as a platform for exploring exotic phases in the wider LnTi$_3$Bi$_4$ (Ln = lanthanide) family of materials.

The kagome motifs, which are composed of two-dimensional honeycomb networks of alternating corner-sharing triangles, are attracting enormous interest as they provide a fascinating platform for exploring the emergence of many topological and correlated electronic phenomenon[1–3]. The kagome structure allows the possibility of flat bands, Dirac-like dispersions, and van Hove singularities (vHSs), resulting in a complex interplay of geometry, topology, and electronic correlation effects[4–18]. For example, a class of kagome superconductors, AV$_3$Sb$_5$ (A = K, Rb, and Cs), was discovered recently and found to host non-trivial band topology, charge density wave order and a superconducting ground state[19–29].

The intertwining of magnetism with the electronic states in the kagome materials has yielded notable discoveries such as the massive Dirac fermions in Fe$_3$Sn$_2$[7], antiferromagnets Mn$_3$Sn and Mn$_3$Ge that showcase giant anomalous Hall effect[30,31] and the Weyl semimetal state in Co$_3$Sn$_2$S$_2$[32,33]. The RMn$_6$Sn$_6$ kagome family (R = rare-earth element) has garnered special attention due to its unique magnetic tunability and large Berry curvature fields[10,14,34–43]. TbMn$_6$Sn$_6$ hosts massive Dirac fermions at the K point owing to Landau quantization and the presence of Landau fan diagram[10,34]. Flat bands and Dirac fermions have been reported in RMn$_6$Sn$_6$ (R = Gd–Dy, Y)[14,35,36] family, topological Hall effect has been observed in YMn$_6$Sn$_6$, ErMn$_6$Sn$_6$, and HoMn$_6$Sn$_6$[39–42], and a large anomalous Hall effect has been reported in LiMn$_6$Sn$_6$[44].

Recently, two kagome metals, YbV$_3$Sb$_4$ and EuV$_3$Sb$_4$, were reported, introducing a new family of vanadium-based kagome materials[45]. It was found that YbV$_3$Sb$_4$ is a Pauli paramagnet with no clear thermodynamic phase transition between 300 K and 60 mK, whereas EuV$_3$Sb$_4$ displays a ferromagnetic transition below T_c of roughly 32 K and a signature of spin-texture under low-fields. The larger LnM$_3$X$_4$ (MX: VSb, TiBi) family is growing rapidly[46,47], providing a new kagome materials platform.

Here we discuss our comprehensive investigation of the electronic structure of the YbTi$_3$Bi$_4$ kagome material. Our approach involves magneto-transport and angle-resolved photoemission spectroscopy (ARPES) measurements, in combination with parallel density-functional theory (DFT) based calculations. YbTi$_3$Bi$_4$, like its structural analog YbV$_3$Sb$_4$ is a nonmagnetic (Yb^{2+}) kagome metal, which does not exhibit any electronic or structural phase transitions down to 60 mK[47]. Our ARPES measurements on YbTi$_3$Bi$_4$ indicate the presence of several flat bands spanning a large area of the Brillouin zone (BZ), multiple vHSs at the $\overline{\mathrm{M}}$ point, and a linear Dirac-like state at the $\overline{\mathrm{K}}$ symmetry point, and are consistent with our DFT calculations. Our study establishes YbTi$_3$Bi$_4$ as a fertile playground for exploring exotic physics in an easily exfoliable Ti-based nonmagnetic kagome material.

Results

YbTi$_3$Bi$_4$ crystallizes in the orthorhombic space group $Fmmm$ (No. 69) with a = 5.91(4) Å, b = 10.3(4) Å, c = 24.9(4) Å, and $\alpha = \beta = \gamma = 90°$. Figure 1a, b shows that the structure consists of Ti kagome layers stacked along the c-axis between the Bi and Yb layers. To emphasize the kagome lattice formed by

[1]Department of Physics, University of Central Florida, Orlando, FL, USA. [2]Materials Science and Technology Division, Oak Ridge National Laboratory, Oak Ridge, TN, USA. [3]Department of Physics, Northeastern University, Boston, MA, USA. [4]Quantum Materials and Sensing Institute, Northeastern University, Burlington, MA, USA. [5]Department of Materials Science and Engineering, The University of Tennessee, Knoxville, TN, USA. [6]Department of Physics and Astronomy, University of Tennessee Knoxville, Knoxville, TN, USA. [7]These authors contributed equally: Anup Pradhan Sakhya, Brenden R. Ortiz, Barun Ghosh. ✉e-mail: madhab.neupane@ucf.edu
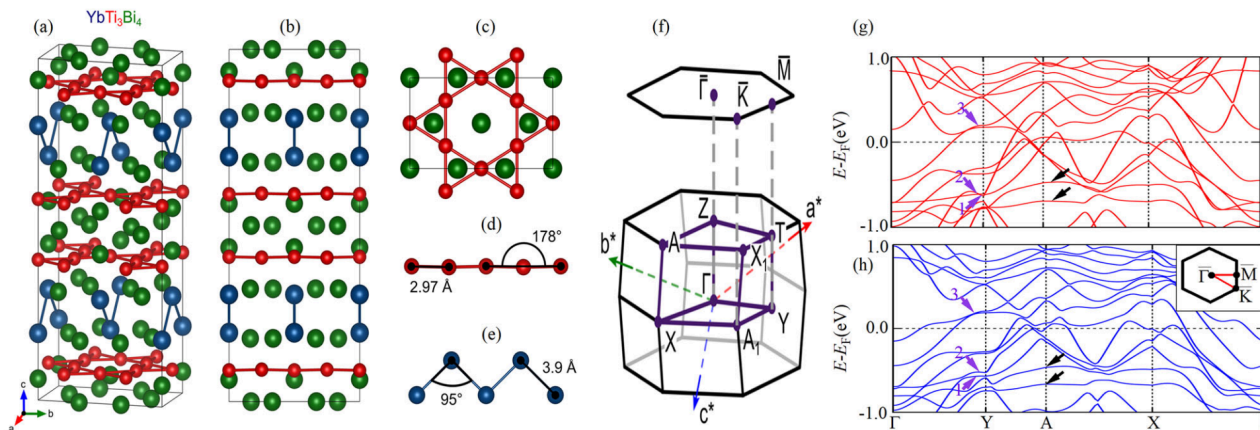
Fig. 1 | Crystal structure and DFT results for YbTi$_3$Bi$_4$. a Crystal structure of YbTi$_3$Bi$_4$ where the blue, red, and green solid spheres denote Yb, Ti, and Bi atoms, respectively. The crystal structure is orthorhombic *(Fmmm)* with a zig-zag sublattice of Yb atoms. **b** The kagome lattice, which is formed by the Ti atoms, **c** is slightly distorted and it is not coplanar. **d** A view of the structure perpendicular to the *b–c* plane, which highlights the relatively small out-of-plane distortion of about (~2°).

e Zig-zag chain formed by the Yb atoms. **f** Bulk Brillouin zone (BZ) and its projection onto the (001) surface BZ; high-symmetry points are marked. **g** DFT-based energy bands along the various high-symmetry directions without the inclusion of spin–orbit coupling (SOC). **h** Same as (**g**) except that these results include SOC. Purple and black arrows in (**g** and **h**) point to vHSs and flat bands, respectively.
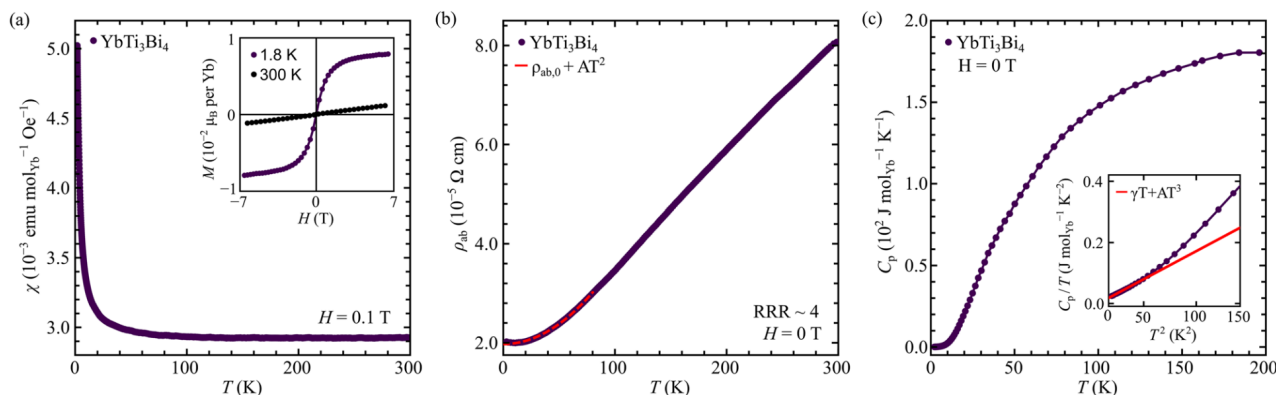
Fig. 2 | Bulk electronic properties and characterization of a YbTi$_3$Bi$_4$ single crystal specimen. a Magnetic susceptibility (χ) versus temperature under a magnetic field of H = 0.1 T. Inset shows magnetization as a function of magnetic field M(H) up

to 7 T at 300 and 1.8 K. **b** Temperature-dependent zero-field electrical resistivity. **c** Temperature dependence of the specific heat (C_p) over 2–300 K. Inset highlights C_p/T versus T^2 in the low-temperature regime.

the Ti atoms and the zig-zag chains formed by the Yb atoms, we highlight only the Ti–Ti, and Yb–Yb bonds in Fig. 1. Kagome layers formed by the Ti atoms are better visualized in Fig. 1c, where each unit cell consists of four kagome layers. However, unlike AV_3Sb_5, the kagome layers formed by the Ti atoms in YbTi$_3$Bi$_4$ exhibit slight buckling (Fig. 1b, d). Figure 1e illustrates the zig-zag chains formed by the Yb atoms extending in the *a*-direction. The Yb–Yb distance in the chains is ~3.9 Å, which is significantly shorter than the nearest neighbor Yb–Yb interchain distance of ~5.7 Å.

The bulk BZ and its projection on the (001) surface (labeled with the pseudo-hexagonal $\overline{M}$, $\overline{K}$, and $\overline{\Gamma}$ nomenclature) is presented in Fig. 1f. To gain insight into the electronic structure of YbTi$_3$Bi$_4$, we performed band structure calculations without (Fig. 1g) and with the inclusion of the spin–orbit coupling effects (Fig. 1h); see Supplementary Note 1 and Supplementary Fig. 1 for orbital-resolved band structures. Multiple bands are seen to cross the Fermi level (E_F) consistent with the metallic nature of YbTi$_3$Bi$_4$. Effects of SOC are generally small, except for the Dirac-like crossing along the Γ–X direction which becomes gapped with the inclusion of SOC. We observe three vHS points at Y (purple arrows) along with the presence of dispersionless bands below the E_F (black arrows), indicating a high degree of localization of the associated electronic states. The dispersionless or "flat" bands are seen to extend over a large portion of the BZ. The flat bands at ~ -0.5 eV and ~ -0.7 eV predominantly arise from the

kagome-based Ti d_{xy} and $d_{x^2-y^2}$ orbitals, see Supplementary Note 1 and Supplementary Fig. 1.

For experimental work, we grew high-quality single crystals of YbTi$_3$Bi$_4$ using the flux method. Temperature-dependent molar magnetic susceptibility $\chi(T) = \mathbf{M/H}$ measured under magnetic field of $\mathbf{H} = 0.1$ T is presented in Fig. 2a for $\mathbf{H} \parallel c$. Essentially temperature-independent Pauli paramagnetism is seen with a weak Curie tail from the impurity spins. The extremely weak nature of the susceptibility (10^{-3} emu Oe^{-1} mol^{-1}) is evident from Fig. 2a, which does not display any signature of a bulk magnetic moment. No qualitative difference is observed when $\mathbf{H}$ is applied $\parallel$ versus $\perp$ to the c-axis. The inset compares magnetization as a function of the magnetic field at 300 and 1.8 K, and shows no saturation up to 7 T. Note that the scale of the $\mathbf{M}$ versus $\mathbf{H}$ plot is of the order of 10^{-2} μ_B per Yb, consistent with the polarization of impurity spins.

Figure 2b shows the electrical resistivity ρ as a function of temperature, where the current is flowing in the *ab*-plane. The typical metallic behavior is seen until the lowest temperature of 2 K used in the measurements. The residual resistivity is ~20 μΩ cm and the residual resistivity ratio is around 4. The resistivity data at low temperatures (<80 K) is modeled using the Fermi liquid picture, which yields the simple quadratic form, $\rho = \rho_0 + aT^2$ (red dotted line), where $\rho_0 = 19.7$ μΩ cm and $a = 1.6 \times 10^{-3}$ μΩ cm K^{-2}. We also measured the specific heat (C_p) of the sample from 200 K down to 2 K
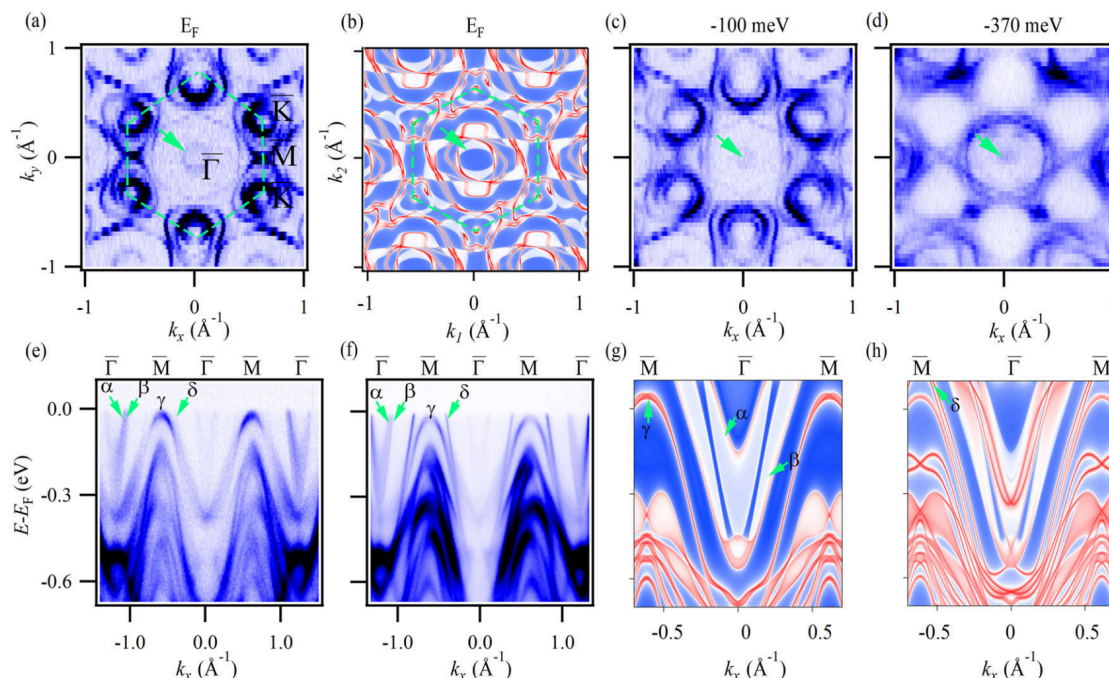
Fig. 3 | Fermi surface (FS) and band dispersion along the $\overline{M}$–$\overline{\Gamma}$–$\overline{M}$ high-symmetry line. a ARPES measured FS using a photon energy of 90 eV. High-symmetry points are labeled. **b** DFT calculated FS. **c**, **d** Constant-energy contours at various binding energies as noted on the top of each plot. **e** Experimental band dispersion measured along the $\overline{\Gamma}$–$\overline{M}$–$\overline{\Gamma}$–$\overline{M}$–$\overline{\Gamma}$ high-symmetry line with a photon energy of 90 eV. **f** Same as (**e**) except that the measurements are with a photon energy of 75 eV. **g** Projected bulk band structure along the $\overline{M}$–$\overline{\Gamma}$–$\overline{M}$ high-symmetry line. **h** Same as (**g**) except that this panel includes the surface states.

without a magnetic field (Fig. 2c). We have fitted the C_p data over the limited temperature range of 2–12 K using the Sommerfeld model. Recall that the C_p for nonmagnetic metals consists of of electronic C_e and lattice C_{ph} contributions, and at low temperature it is given by: $C_p(T) = \gamma T + \beta T^3$, where $C_e = \gamma T$ and $C_{ph} = \beta T^3$. Here, γ is the Sommerfeld coefficient, and $\beta = 12\pi^4 NR/5\Theta_D^3$ with N, R, and Θ_D representing the number of atoms per unit cell, the ideal gas constant, and the Debye temperature, respectively. The inset of Fig. 2c shows that the $C_p/(T)$ scales linearly with T^2 at low temperatures. The resulting least-squares fit yields the parameters $\gamma = 1.78 \times 10^{-2}$ J mol^{-1} K^{-2} and $\beta = 1.46 \times 10^{-3}$ J mol^{-1} K^{-4}. These results indicate that YbTi$_3$Bi$_4$ is a nonmagnetic kagome metal with no clear thermodynamic phase transitions up to 300 K.

We turn now to discuss our ARPES measurements from YbTi$_3$Bi$_4$. Note that our DFT calculations indicate that the density of states (DOS) at the E_F in YbTi$_3$Bi$_4$ is dominated by the Ti and Bi orbitals. With the Yb-orbitals lying away from the E_F, ARPES is expected to show an apparent sixfold symmetry, although the underlying structure is orthorhombic. We focus first on the Fermi surface (FS) topology. Figure 3a presents the FS measured using a photon energy of 90 eV as a function of k_x and k_y. Several pockets can be seen at the E_F, with a circular pocket near the BZ center $\overline{\Gamma}$, a pocket with hexagonal symmetry which is anticipated due to the underlying symmetry of the kagome lattice along the $\overline{\Gamma}$–$\overline{M}$ direction, and two pockets around the $\overline{K}$ point, where the inner pocket seems to show a circular shape and the outer pocket is triangular; see Supplementary Note 2 and Supplementary Fig. 2a for additional results of FS measurements. The DFT-based bulk FS including surface states, presented in Fig. 3b, is in good agreement with our experimental results, see Supplementary Note 2 and Supplementary Fig. 2b for bulk FS without the surface states. Discrepancies between the theory and experiment may be attributed to the effects of the ARPES matrix element[48,49] and the intrinsic limitations of the DFT in capturing electronic correlations[50–52].

ARPES measured constant-energy contours (CECs) are presented in Fig. 3c, d at various binding energies. With increasing binding energy, the circular pocket at $\overline{\Gamma}$ contracts to a point-like feature around ~ -370 meV

indicating its electron-like nature, whereas the pocket at $\overline{K}/\overline{M}$ increases in size with increasing binding energy, indicating its hole-like nature. Note that the underlying orthorhombic structure naturally imparts small distortions to the kagome lattice, which result in the apparent sixfold symmetry in the ARPES FS and CECs. Although we refer to the data using the hexagonal nomenclature, the underlying symmetry is twofold.

Band dispersions along the $\overline{\Gamma}$–$\overline{M}$–$\overline{\Gamma}$–$\overline{M}$–$\overline{\Gamma}$ high-symmetry line using photon energies of 90 and 75 eV are shown in Fig. 3e and f, respectively. In agreement with our measured FS and CECs, an electron-like pocket can be seen at the $\overline{\Gamma}$ point. However, a closer examination of the band dispersion at $\overline{\Gamma}$ in the second BZ reveals the presence of two distinct pockets. This is also evident in the band-dispersion plot obtained with 75 eV photons along the $\overline{\Gamma}$–$\overline{M}$–$\overline{\Gamma}$–$\overline{M}$–$\overline{\Gamma}$ line, see Fig. 3f. [For detailed analysis of the bands, labeled α and β, see Supplementary Note 3 and Supplementary Fig. 3a, b]. We also obtained momentum distribution curves (MDCs) by integrating over an energy window of 10 meV below the Fermi level around the $\overline{\Gamma}$ point in the second BZ and fitted the spectra using two Gaussian peaks (see Supplementary Note 3 and Supplementary Fig. 3c) to further confirm the presence of two peaks (α and β) at $\overline{\Gamma}$. Additionally, two hole-like bands (γ and δ) are visible in Fig. 3e, f, which exhibit hole-like characteristics consistent with the FSs and CECs presented in Fig. 3a, c, d. Our projected (bulk) DFT calculations in Fig. 3g are in good agreement with the results of ARPES measurements in Fig. 3e, f, reproducing the two electron-like pockets α and β, and the hole-like pocket around the γ point, indicating their bulk origin. However, the band denoted as δ in the ARPES spectra is not reproduced in our DFT calculations. When surface states are included in the calculations, Fig. 3h shows the appearance of the hole-like pocket δ (green arrow), suggesting its surface origin.

Figure 4a presents the experimental ARPES band structure along $\overline{\Gamma}$–$\overline{M}$–$\overline{K}$–$\overline{\Gamma}$. The most prominent feature is the presence of the vHSs, denoted vHS1 and vHS2 (purple arrows), along with four dispersionless flat bands (black arrows) that extend across a large region of the BZ, which lie at binding energies of ~ -0.3 eV, ~ -0.5 eV, ~ -0.7 eV, and ~ -1.1 eV. The flat bands at ~ -0.3 eV and ~ -0.5 eV are attributed to the destructive
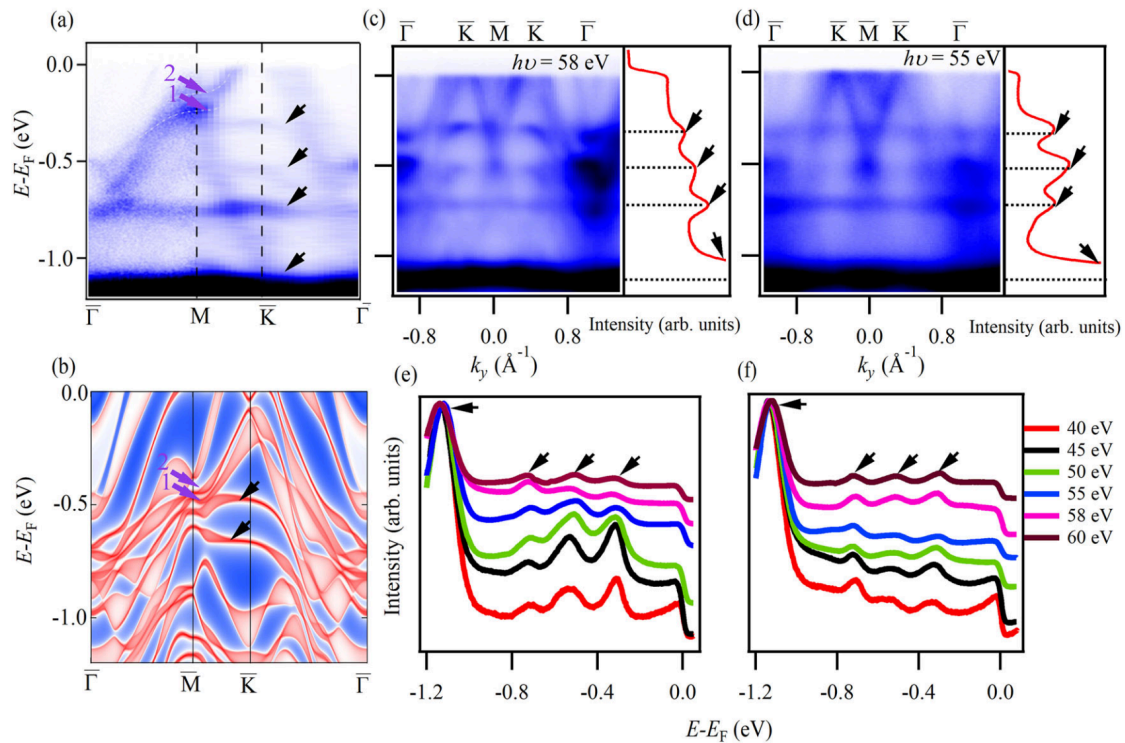
Fig. 4 | Visualization of multiple vHSs and flat bands. a Experimental photo-electron intensity plot of the band structure along the $\overline{\Gamma}-\overline{M}-\overline{K}-\overline{\Gamma}$ line with 90 eV photons. The white-dashed curves serve as guides to the eye to help visualize the two vHSs. Purple and black arrows in (**a**) and (**b**) point to the vHSs and flat bands, respectively. **b** DFT-based bulk band structure along the $\overline{\Gamma}-\overline{M}-\overline{K}-\overline{\Gamma}$ line. **c** Experimental band dispersion and the associated integrated energy distribution curves (EDCs) along the $\overline{\Gamma}-\overline{K}-\overline{M}-\overline{K}-\overline{\Gamma}$ line measured using 58 eV photons. Peak positions in the EDCs (black arrows) denote flat bands at ~ -0.3 eV, ~ -0.5 eV, and ~ -0.7 eV, with the most intense peak lying at around ~ -1.1 eV. **d** Same as (**c**)

except these results are for measurements using 55 eV photons. **e** Integrated intensity of the EDCs (over the momentum range of -0.8 Å^{-1} to 0.8 Å^{-1}) along the $\overline{\Gamma}-\overline{K}-\overline{M}-\overline{K}-\overline{\Gamma}$ line. The EDCs used to obtain integrated intensities plotted were taken at photon energies ranging from 40 to 60 eV as indicated by the color bars on the right side of (**f**). Peak positions in the EDCs (black arrows) correspond to flat bands. **f** Same as (**e**) except that here the integration involves EDCs along the $\overline{K}-\overline{\Gamma}-\overline{K}$ line.

interference of wavefunctions within the Ti kagome motif, with interlayer coupling between the two kagome layers resulting in bonding (with a decreased energy at around ~ -0.5 eV) and antibonding (with an increased energy at around ~ -0.3 eV) splittings[7,53]. Orbital-resolved DFT calculations suggest that these flat bands predominantly consist of a mixture of Ti d_{xy} and Ti $d_{x^2-y^2}$ orbitals, see Supplementary Note 1 and Supplementary Fig. 1. The discrepancy of ~200 meV between the DFT calculations and the ARPES results may be due to the neglect of Yb $4f$ states in our calculations[48–52]. The flat band observed at ~ -0.7 eV is associated with Yb surface atoms, while the flat band around ~ -1.1 eV originates from bulk Yb^{2+} $4f_{5/2}$ states[54], see Supplementary Note 4 and Supplementary Fig. 4 for additional photon energy dependent measurements. vHS2 mostly involves Ti $d_{x^2-y^2}$ and Ti d_{z^2} orbitals, whereas vHS1 mainly involves the Ti d_{xy} orbital. The vHS above the E_F seen in DFT calculations, which is not accessible to ARPES, mostly consists of Ti d_{xy} orbital, see Supplementary Note 1 and Supplementary Fig. 1. Except for the flat bands contributed by Yb $4f$ states, the DFT calculated bulk band structure along $\overline{\Gamma}-\overline{M}-\overline{K}-\overline{\Gamma}$ in Fig. 4b reproduces the ARPES measured vHSs (vHS1 and vHS2) and flat bands. The vHSs near the E_F have been implicated in driving exotic physics (e.g., charge ordering and superconductivity) in AV$_3$Sb$_5$ (A = K, Rb, and Cs) kagome metals. Since the vHSs in YbTi$_3$Bi$_4$ lie away from the E_F, this could explain the absence of charge ordering and superconductivity in this material.

To further examine the flat bands, we present the band dispersion along $\overline{\Gamma}-\overline{K}-\overline{M}-\overline{K}-\overline{\Gamma}$ high-symmetry using 58 and 55 eV photons in Fig. 4c and d, respectively. Four dispersionless bands at binding energies of ~ -0.3 eV, ~ -0.5 eV, ~ -0.7 eV, and ~ -1.1 eV can be seen as before at both photon energies. The associated DOS can be visualized by examining

the momentum-integrated EDCs in Fig. 4c and d, which exhibit several distinct peaks (black arrows) that arise from flat bands. Figure 4e, f shows the momentum-integrated EDCs as a function of photon energy along $\overline{\Gamma}-\overline{K}-\overline{M}-\overline{K}-\overline{\Gamma}$ and $\overline{K}-\overline{\Gamma}-\overline{K}$; see Supplementary Note 4 and Supplementary Figs. 5, 6 for additional data. The peaks related to the four flat bands in these integrated spectra also occur at the four aforementioned energies, as expected (black arrows). A closer examination of the spectra reveals a slight dispersion in the flat bands around ~ -0.3 eV and ~ -0.5 eV, which could be attributed to hopping between the nearest and/or next-nearest-neighbor atoms within the same or adjacent kagome planes[53].

It is interesting to further consider band dispersions along $\overline{K}-\overline{\Gamma}-\overline{K}$. Results at 50 and 60 eV photon energies presented in Fig. 5a, b show the presence of a linear Dirac-like state formed by the innermost band (dashed blue lines culminating in the blue arrow), which looks like a hole pocket that merges near the E_F. For additional related ARPES results, see Supplementary Note 4 and Supplementary Fig. 6. The linear Dirac-like band is better resolved at 60 eV photon energy and is identified by symbol ζ for clarity. The asymmetry seen in the spectra around $\overline{K}$ is likely due to well-known photoemission cross-section effects, in ARPES measurements. To gain further insight into the nature of the innermost linear Dirac-like band (blue arrow in Fig. 5a, b), we consider MDCs obtained by integrating the spectra over a narrow 10 meV binding energy range below the Fermi level. The results obtained from spectra taken at various photon energies are presented in Supplementary Notes 4, 5 and Supplementary Figs. 6, 7. The innermost band at the $\overline{K}$ is seen to show dispersion, indicating its bulk origin, see Supplementary Note 5 and Supplementary Fig. 7 for details. The bulk bands plotted in Fig. 5c also show a linear Dirac-like band around the $\overline{K}$ point (blue arrow) in reasonable accord with our experimental results. The band
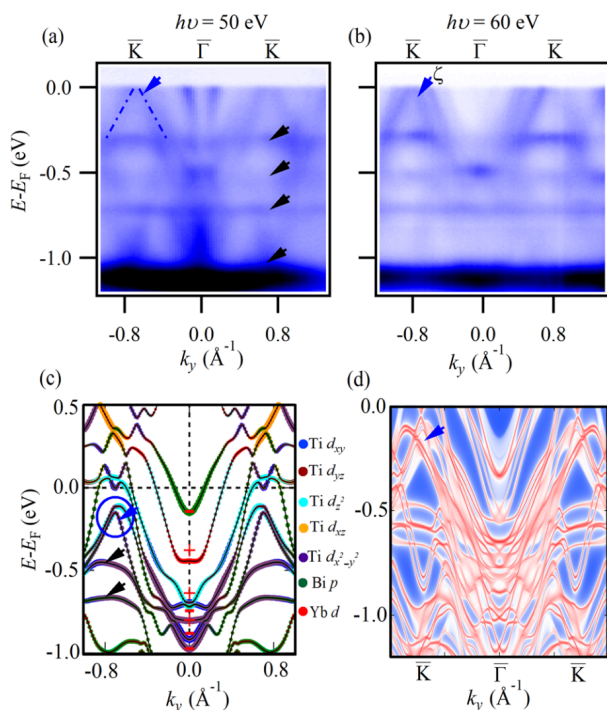
Fig. 5 | Observation of a Dirac-like state at the $\overline{K}$ point. Experimental band dispersions along $\overline{K}$–$\overline{\Gamma}$–$\overline{K}$ using a photon energy of **a** 50 eV, and **b** 60 eV. **c** Orbital-projected bulk band structure along $\overline{K}$–$\overline{\Gamma}$–$\overline{K}$. Color scale provides relative contributions from various orbitals. **d** DFT-based (bulk) projected band structure including the surface states.

characters in Fig. 5c indicate that the linear Dirac-like state is dominated by the Ti $d_{x^2-y^2}$ orbitals.

Interestingly, there are many band inversions in the bulk band structure of Fig. 5c. To unravel the topology of YbTi$_3$Bi$_4$, we have calculated the Z_2 invariant by following the evolution of the Wannier charge center and also via the parity-based methods, see Supplementary Fig. 8. In this way, we found the strong Z_2 invariant to vanish ($\nu_0 = 0$) and the weak invariants to be: $\nu_1 = 0$, $\nu_2 = 1$, $\nu_3 = 1$. Figure 5d presents a DFT-based projection in which both the bulk and surface bands are included. These results are in line with much of the discussion above of bulk and surface states and their signatures in the experimental ARPES spectra, and exhibit complex hybridization of the bulk and surface states at the $\overline{K}$ point, see Supplementary Note 6 and Supplementary Fig. 9 for further details.

Discussion

Defining features of the valence electronic structure of YbTi$_3$Bi$_4$ include: (i) a linear Dirac-like state near E_F at the $\overline{K}$ point; (ii) based on DFT calculations, a saddle-point vHS at $\overline{M}$ lying about 150 meV above E_F, along with other two vHSs about 250 meV below the E_F; and (iii) four flat bands spanning across a large region of the BZ, with two of these originating from Yb $4f$ states and the other two from the Ti $3d$ kagome states. These features should be contrasted with the low-energy electronic spectrum of vanadium-based kagome materials such as AV$_3$Sb$_5$ in which the physics responsible for producing exotic phenomena, such as superconductivity, is dominated by the interplay of the saddle-point vHSs and a topological surface state, both located at $\overline{M}$ in close proximity to the E_F[55–58]. Absence of vHSs near E_F could be the reason for lack of superconductivity and charge ordering in YbTi$_3$Bi$_4$. Flat bands have been predicted theoretically in AV$_3$Sb$_5$: one flat band lies about 1 eV above the E_F (inaccessible to ARPES), while the other flat band around 1.2 eV below E_F is not well resolved in ARPES experiments[20,58]. In contrast, we have clearly shown the presence of several flat bands in YbTi$_3$Bi$_4$. It should be possible to tune the chemical potential in YbTi$_3$Bi$_4$ so that it lies near the vHSs and the flat bands. Magnetism in YbTi$_3$Bi$_4$ can also

be tuned by replacing Yb with other rare-earth elements[47]. Our work thus sets the stage for further exploration of YbTi$_3$Bi$_4$, including studies involving its exfoliation down to few monolayers.

Conclusions

In summary, we have synthesized a nonmagnetic Ti-based kagome material (YbTi$_3$Bi$_4$) and analyzed its electronic structure in-depth using a combination of magneto-transport, ARPES, and parallel first-principles calculations. The ARPES measured FS and band dispersions are in good accord with our theoretical predictions. We provide compelling evidence for the presence of multiple flat bands and vHSs in YbTi$_3$Bi$_4$. The flat bands originate from both the Ti-based kagome lattice and the Yb^{2+}$4f$ orbitals. Our work highlights the importance of the Ti-based LnTi$_3$Bi$_4$ kagome family as a potential platform for exploring exotic phases.

Note added to proof

While the manuscript was under review, several related studies have been published[47,59–61].

Methods

Experimental details

YbTi$_3$Bi$_4$ single crystals were grown through bismuth self-flux. Elemental reagents of Yb (Alfa 99.9%), Ti (Alfa 99.9% powder), and Bi (Alfa 99.999% low-oxide shot) were combined in 2:3:12 ratio into 2 mL Canfield crucibles fitted with a catch crucible and a porous frit[62]. The crucibles were sealed under ~0.7 atm of argon gas in fused silica ampoules. Each composition was heated to 1050 °C at a rate of 200 °C/h. Samples were allowed to thermalize and homogenize at 1050 °C for 12–18 h before cooling to 500 °C at a rate of 2 °C/h. Excess bismuth was removed through centrifugation at 500 °C.

Synchrotron-based ARPES experiments were performed at the ALS beamlines 10.0.1.1 and 4.0.3 at a temperature of 15 K equipped with R4000 and R8000 hemispherical electron analyzers. Additional ARPES experiments were carried out at the Stanford Synchrotron Radiation Lightsource end station 5-2 at 15 K. The angular and energy resolution were set at better than 0.2° and 15 meV, respectively. High-quality single crystals were cut into small pieces and mounted on a copper post using silver epoxy. Ceramic posts were attached on top of the samples. To avoid oxidation, samples were prepared in a glove box, and loaded into the main chamber which was cooled and pumped down for a few hours. Measurements were carried out at 11 K. Pressure in the UHV chamber was maintained at around 10^{-11} Torr.

Computational methods

Electronic structure calculations were performed within the DFT framework using a plane-wave basis set as implemented in the Vienna Ab initio Simulation Package (VASP)[63,64]. Standard projector-augmented-wave (PAW) pseudopotentials were used[65]. The kinetic energy cutoff for the plane-wave basis was set to 500 eV. A Γ-centered $10 \times 10 \times 10$ k mesh was used for k-space integrations. The SCAN (strongly-constrained and appropriately-normed) functional was used to treat exchange-correlation effects[66,67]. Yb_3 pseudopotential was used, where the Yb $4f$ electrons are taken to be core electrons. The lattice parameters were fully relaxed by optimizing atomic positions until the force on each atom became less than 0.001 eV Å. The relaxed lattice parameters are $a = 5.862$ Å, $b = 10.385$ Å, $c = 24.838$ Å, which are very close to the corresponding experimental values.

Data availability

The data that support the findings of this study are available within the manuscript and the Supplementary Information. Other findings of this study are available from the corresponding author upon reasonable request.

References

1. Syôzi, I. Statistics of kagomé lattice. *Prog. Theor. Phys.* **6**, 306 (1951).

2. Zhou, Y., Kanoda, K. & Ng, T.-K. Quantum spin liquid states. *Rev. Mod. Phys.* **89**, 025003 (2017).

3. Neupert, T., Denner, M. M., Yin, J.-X., Thomale, R. & Hasan, M. Z. Charge order and superconductivity in kagome materials. *Nat. Phys.* **18**, 137 (2022).

4. Guo, H.-M. & Franz, M. Topological insulator on the kagome lattice. *Phys. Rev. B* **80**, 113102 (2009).

5. Tang, E., Mei, J.-W. & Wen, X.-G. High-temperature fractional quantum Hall states. *Phys. Rev. Lett.* **106**, 236802 (2011).

6. Han, T.-H. et al. Fractionalized excitations in the spin-liquid state of a kagome-lattice antiferromagnet. *Nature* **492**, 406 (2012).

7. Ye, L. et al. Massive Dirac fermions in a ferromagnetic kagome metal. *Nature* **555**, 638 (2018).

8. Lin, Z. et al. Flatbands and emergent ferromagnetic ordering in Fe_3Sn_2 kagome lattices. *Phys. Rev. Lett.* **121**, 096401 (2018).

9. Yin, J.-X. et al. Negative flat band magnetism in a spin-orbit-coupled correlated kagome magnet. *Nat. Phys.* **15**, 443 (2019).

10. Yin, J.-X. et al. Quantum-limit Chern topological magnetism in $TbMn_6Sn_6$. *Nature* **583**, 533 (2020).

11. Kang, M. et al. Dirac fermions and flat bands in the ideal kagome metal FeSn. *Nat. Mater.* **19**, 163 (2020).

12. Kang, M. et al. Topological flat bands in frustrated kagome lattice CoSn. *Nat. Commun.* **11**, 4004 (2020).

13. Ghimire, N. J. & Mazin, I. I. Topology and correlations on the kagome lattice. *Nat. Mater.* **19**, 137 (2020).

14. Li, M. et al. Dirac cone, flat band and saddle point in kagome magnet YMn_6Sn_6. *Nat. Commun.* **12**, 3129 (2021).

15. Regmi, S. et al. Spectroscopic evidence of flat bands in breathing kagome semiconductor Nb_3I_8. *Commun. Mater.* **3**, 100 (2022).

16. Yin, J.-X., Lian, B. & Hasan, M. Z. Topological kagome magnets and superconductors. *Nature* **612**, 647 (2022).

17. Balents, L. Spin liquids in frustrated magnets. *Nature* **464**, 199 (2010).

18. Yang, J. et al. Observation of flat band, Dirac nodal lines and topological surface states in Kagome superconductor $CsTi_3Bi_5$. *Nat. Commun.* **14**, 4089 (2023).

19. Ortiz, B. R. et al. New kagome prototype materials: discovery of KV_3Sb_5, RbV_3Sb_5, and CsV_3Sb_5. *Phys. Rev. Mater.* **3**, 094407 (2019).

20. Ortiz, B. R. et al. CsV_3Sb_5: A Z_2 topological kagome metal with a superconducting ground state. *Phys. Rev. Lett.* **125**, 247002 (2020).

21. Ortiz, B. R. et al. Superconductivity in the Z_2 kagome metal KV_3Sb_5. *Phys. Rev. Mater.* **5**, 034801 (2021).

22. Ortiz, B. R. et al. Fermi surface mapping and the nature of charge-density-wave order in the kagome superconductor CsV_3Sb_5. *Phys. Rev. X* **11**, 041030 (2021).

23. Zhao, H. et al. Cascade of correlated electron states in the kagome superconductor CsV_3Sb_5. *Nature* **599**, 216 (2021).

24. Hu, Y. et al. Coexistence of trihexagonal and star-of-David pattern in the charge density wave of the kagome superconductor AV_3Sb_5. *Phys. Rev. B* **106**, L241106 (2022).

25. Jiang, Y.-X. et al. Unconventional chiral charge order in kagome superconductor KV_3Sb_5. *Nat. Mater.* **20**, 1353 (2021).

26. Hao, Z. et al. Dirac nodal lines and nodal loops in the topological kagome superconductor CsV_3Sb_5. *Phys. Rev. B* **106**, L081101 (2022).

27. Yin, Q. et al. Superconductivity and normal-state properties of kagome metal RbV_3Sb_5 single crystals. *Chin. Phys. Lett.* **38**, 037403 (2021).

28. Luo, H. et al. Electronic nature of charge density wave and electron-phonon coupling in kagome superconductor KV_3Sb_5. *Nat. Commun.* **13**, 273 (2022).

29. Wilson, S. D. & Ortiz, B. R. AV_3Sb_5 kagome superconductors. *Nat. Rev. Mater.* **9**, 420 (2024).

30. Nakatsuji, S., Kiyohara, N. & Higo, T. Large anomalous Hall effect in a non-collinear antiferromagnet at room temperature. *Nature* **527**, 212 (2015).

31. Nayak, A. K. et al. Large anomalous Hall effect driven by a nonvanishing Berry curvature in the noncolinear antiferromagnet Mn_3Ge. *Sci. Adv.* **2**, e1501870 (2016).

32. Liu, E. et al. Giant anomalous Hall effect in a ferromagnetic kagome-lattice semimetal. *Nat. Phys.* **14**, 1125 (2018).

33. Liu, D. F. et al. Magnetic Weyl semimetal phase in a Kagomé crystal. *Science* **365**, 1282 (2019).

34. Ma, W. et al. Rare earth engineering in RMn_6Sn_6 (R=Gd-Tm, Lu) topological kagome magnets. *Phys. Rev. Lett.* **126**, 246602 (2021).

35. Li, R. S. et al. Flat optical conductivity in the topological kagome magnet $TbMn_6Sn_6$. *Phys. Rev. B* **107**, 045115 (2023).

36. Gu, X. et al. Robust kagome electronic structure in the topological quantum magnets XMn_6Sn_6 (X = Dy, Tb, Gd, Y). *Phys. Rev. B* **105**, 155108 (2022).

37. Asaba, T. et al. Anomalous Hall effect in the kagome ferrimagnet $GdMn_6Sn_6$. *Phys. Rev. B* **101**, 174415 (2020).

38. Zeng, H. et al. Large anomalous Hall effect in kagomé ferrimagnetic $HoMn_6Sn_6$ single crystal. *J. Alloys Compd.* **899**, 163356 (2022).

39. Ghimire, N. J. et al. Competing magnetic phases and fluctuation-driven scalar spin chirality in the kagome metal YMn_6Sn_6. *Sci. Adv.* **6**, eabe2680 (2020).

40. Dhakal, G. et al. Anisotropically large anomalous and topological Hall effect in a kagome magnet. *Phys. Rev. B* **104**, L161115 (2021).

41. Wang, Q. et al. Field-induced topological Hall effect and double-fan spin structure with a c-axis component in the metallic kagome antiferromagnetic compound YMn_6Sn_6. *Phys. Rev. B* **103**, 014416 (2021).

42. Kabir, F. et al. Unusual magnetic and transport properties in $HoMn_6Sn_6$ kagome magnet. *Phys. Rev. Mater.* **6**, 064404 (2022).

43. Lv, B. et al. Anomalous Hall effect in kagome ferromagnet $YbMn_6Sn_6$ single crystal. *J. Alloys Compd.* **957**, 170356 (2023).

44. Chen, D. et al. *Phys. Rev. B* **103**, 144410 https://doi.org/10.1103/PhysRevB.103.144410 (2021).

45. Ortiz, B. R. et al. YbV_3Sb_4 and EuV_3Sb_4 vanadium-based kagome metals with Yb^{2+} and Eu^{2+} zigzag chains. *Phys. Rev. Mater.* **7**, 064201 (2023).

46. Ovchinnikov, A. & Bobev, S. Synthesis, crystal and electronic structure of the titanium bismuthides $Sr_5Ti_{12}Bi_{19+x}$, $Ba_5Ti_{12}Bi_{19+x}$, and $Sr_{5-\delta}Eu_\delta Ti_{12}Bi_{19+x}$ ($x \approx 0.5$–1.0; $\delta \approx 2.4$, 4.0). *Eur. J. Inorg. Chem.* **2018**, 1266 (2018).

47. Ortiz, B. R. et al. Evolution of highly anisotropic magnetism in the titanium-based kagome metals $LnTi_3Bi_4$ (Ln: La…Gd^{3+}, Eu^{2+}, Yb^{2+}). *Chem. Mater.* **35**, 9756 (2023).

48. Bansil, A. & Lindroos, M. Importance of matrix elements in the ARPES spectra of BISCO. *Phys. Rev. Lett.* **83**, 5154 (1999).

49. Sahrakorpi, S., Lindroos, M., Markiewicz, R. S. & Bansil, A. Evolution of midgap states and residual three dimensionality in $La_{2-x}Sr_xCuO_4$. *Phys. Rev. Lett.* **95**, 157601 (2005).

50. Sakhya, A. P. et al. Behavior of gapped and ungapped Dirac cones in the antiferromagnetic topological metal SmBi. *Phys. Rev. B* **106**, 085132 (2022).

51. Sakhya, A. P. et al. Complex electronic structure evolution of NdSb across the magnetic transition. *Phys. Rev. B* **106**, 235119 (2022).

52. Sakhya, A. P. et al. Observation of Fermi arcs and Weyl nodes in a noncentrosymmetric magnetic Weyl semimetal. *Phys. Rev. Mater.* **7**, L051202 (2023).

53. Ishii, Y., Harima, H., Okamoto, Y., Yamaura, J.-i & Hiroi, Z. YCr_6Ge_6 as a candidate compound for a kagome metal. *J. Phys. Soc. Jpn.* **82**, 023705 (2013).

54. Wigger, G. et al. Electronic band structure and Kondo coupling in $YbRh_2Si_2$. *Phys. Rev. B* **76**, 035106 (2007).

55. Jiang, K. et al. Kagome superconductors AV_3Sb_5 (A = K, Rb, Cs). *Natl. Sci. Rev.* **10** https://doi.org/10.1093/nsr/nwac199 (2022).

56. Kato, T. et al. Three-dimensional energy gap and origin of charge-density wave in kagome superconductor KV_3Sb_5. *Commun. Mater.* **3**, 30 (2022).

57. Cho, S. et al. Emergence of new van Hove singularities in the charge density wave state of a topological kagome metal RbV_3Sb_5. *Phys. Rev. Lett.* **127**, 236401 (2021).

58. Hu, Y. et al. Topological surface states and flat bands in the kagome superconductor CsV_3Sb_5. *Sci. Bull.* **67**, 495 (2022).

59. Chen, L. et al. Tunable magnetism in titanium-based kagome metals by rare-earth engineering and high pressure. *Commun. Mater.* **5**, 73 (2024).

60. Guo, J. et al. Tunable magnetism and band structure in kagome materials $RETi_3Bi_4$ family with weak interlayer interactions. *Sci. Bull*. https://doi.org/10.1016/j.scib.2024.06.036 (2024).

61. Zheng, Z. et al. Anisotropic magnetism and band evolution induced by ferromagnetic phase transition in titanium-based kagome ferromagnet $SmTi_3Bi_4$. *Sci. China Phys. Mech. Astron.* **67**, 267411 (2024).

62. Canfield, P. C., Kong, T., Kaluarachchi, U. S. & Jo, N. H. Use of frit-disc crucibles for routine and exploratory solution growth of single crystalline samples. *Philos. Mag.* **96**, 84 (2016).

63. Kohn, W. & Sham, L. J. Self-consistent equations including exchange and correlation effects. *Phys. Rev.* **140**, A1133 (1965).

64. Kresse, G. & Furthmüller, J. Efficient iterative schemes for ab initio total-energy calculations using a plane-wave basis set. *Phys. Rev. B* **54**, 11169 (1996).

65. Kresse, G. & Joubert, D. From ultrasoft pseudopotentials to the projector augmented-wave method. *Phys. Rev. B* **59**, 1758 (1999).

66. Sun, J., Ruzsinszky, A. & Perdew, J. P. Strongly constrained and appropriately normed semilocal density functional. *Phys. Rev. Lett.* **115**, 036402 (2015).

67. Sun, J. et al. Accurate first-principles structures and energies of diversely bonded systems from an efficient density functional. *Nat. Chem.* **8**, 831 (2016).

Author contributions

M.N. and B.R.O. conceived the idea. M.N. supervised the project. A.P.S. performed the ARPES measurements with the help of M.S., M.I.M., I.B.E., and N.V.; B.R.O. synthesized the crystals and performed XRD, EDX, magnetic, and transport measurements; D.G.M. provided us valuable insights for transport and spectroscopy measurements; B.G., M.M., and A.B. performed the ab initio density-functional theoretical calculations; A.P.S analyzed the data and wrote the manuscript with input from all the authors; M.N. was responsible for the overall research direction, planning, and integration among different research units. All authors discussed the results, interpretation, and conclusion.

Competing interests

The authors declare no competing interests.

Additional information

Supplementary information The online version contains supplementary material available at https://doi.org/10.1038/s43246-024-00681-3.

Correspondence and requests for materials should be addressed to Madhab Neupane.

Peer review information *Communications Materials* thanks the anonymous reviewers for their contribution to the peer review of this work. Primary handling editor: Aldo Isidori. A peer review file is available.

Reprints and permissions information is available at http://www.nature.com/reprints

Publisher's note Springer Nature remains neutral with regard to jurisdictional claims in published maps and institutional affiliations.